

Observation of space-time surface plasmon polaritons

Naoki Ichiji,^{1,2} Hibiki Kikuchi,³ Murat Yessenov,^{4,5} Kenneth L. Schepler,⁴ Ayman F. Abouraddy,^{4,*} and Atsushi Kubo^{6,†}

¹*Graduate School of Pure and Applied Sciences, University of Tsukuba,
1-1-1 Tennodai, Tsukuba-shi, Ibaraki 305-8571, Japan*

²*Institute of Industrial Science, The University of Tokyo,
4-6-1 Komaba, Meguro-Ku, Tokyo 153-8505, Japan*

³*School of Science and Engineering, University of Tsukuba,
1-1-1 Tennodai, Tsukuba-shi, Ibaraki 305-8571, Japan*

⁴*CREOL, The College of Optics & Photonics, University of Central Florida, Orlando, FL 32816, USA*

⁵*Harvard John A. Paulson School of Engineering and Applied Sciences, Harvard University, Cambridge, MA, USA*

⁶*Institute of Pure and Applied Sciences, University of Tsukuba,
1-1-1 Tennodai, Tsukuba-shi, Ibaraki 305-8571, Japan*

Surface plasmon polaritons (SPPs) are surface-bound waves at metal-dielectric interfaces that exhibit strong out-of-plane field confinement, a key feature for applications is nano-scale sensing and imaging. However, this advantage is offset by diffractive spreading during in-plane propagation, leading to transverse spatial delocalization. Conventional strategies to combat diffraction through spatial structuring are not applicable for dimensionally restricted SPPs – except for cosine plasmons that are not localized or Airy plasmons that propagate along a curved trajectory. Here, we report the first realization of space-time SPPs (ST-SPPs), ultrashort (16 fs) diffraction-free SPPs that propagate in a straight line, whose unique propagation characteristics stem from precise sculpting of their spatiotemporal spectra. By first synthesizing a spatiotemporally structured field in free space, we couple the field to an axially invariant ST-SPP at a metal-dielectric surface via an ultra-broadband nanoslit coupling mechanism, further enabling control over the ST-SPP group velocity and propagation characteristics. Time-resolved two-photon fluorescence interference microscopy enables reconstructing the surface-bound field in space and time, thereby verifying their predicted phase-tilted spatiotemporal wave-front and diffraction-free propagation. Our work opens new avenues for combining spatiotemporally structured light with the field-localization associated with nanophotonics, and may thus enable novel applications in surface-enhanced sensing and nonlinear optical interactions.

INTRODUCTION

Surface plasmon polaritons (SPPs) are optical surface waves that propagate along metal-dielectric interfaces [1, 2]. Because SPPs are strongly localized orthogonally to the interface, they are suitable for a host of photonic applications ranging from biosensing [3] and tweezers [4], to nanofocusing [5, 6], modulators [7–9], and harvesting solar energy [10, 11], among other fascinating possibilities [12–15]. This strong field confinement of the SPP at the interface is marred by free in-plane propagation, resulting in diffractive spreading of its transverse spatial profile. In addition, SPPs are dispersive, so that the temporal (axial) profile of a pulsed SPP undergoes dispersive spreading (Fig. 1a). Producing diffraction-free, tightly focused, ultrashort pulsed SPPs would yield strong field localization in all dimensions that is maintained over extended propagation distances, which can help enhance many SPP applications.

Axially maintained, in-plane confinement can be provided by surface-patterned waveguide structures [16, 17], or by hyperbolic metamaterials that requires strongly anisotropic materials [18–21]. In free space, so-called

diffraction-free optical beams can maintain their spatial profile axially over considerable distances if their profile conforms to particular functional distributions; e.g., Bessel beams [22]. However, the one-dimensional (1D) transverse nature of SPPs is a restrictive condition with regards to achieving diffraction-free propagation. Indeed, there are no monochromatic diffraction-free light sheets – which are localized along one transverse dimension and uniform along the other – that travel in a straight line [23]. Conventional diffraction-free beams require two transverse dimensions for their viability; so that even a light-sheet that conforms to a Bessel function in 1D is diffractive, in contrast to its 2D counterpart. There are only two exceptions: the cosine wave that is not localized, and the Airy beam that does not travel along a straight line [23]. Both of these monochromatic field structures have been implemented as SPPs: the cosine plasmon [24, 25] and the Airy plasmon [26, 27]. Therefore, no diffraction-free SPP traveling along a straight path has been realized to date. This remains a fundamental challenge that cannot be overcome by means of spatially structuring the excitation, which is a consequence of the dimensionality of SPPs as surface waves, along with the monochromaticity of the excitation. Whereas the first restriction cannot be avoided, the second can be readily circumvented by sculpting a *pulsed* SPP wave packet.

* raddy@creol.ucf.edu

† kubo.atsushi.ka@u.tsukuba.ac.jp

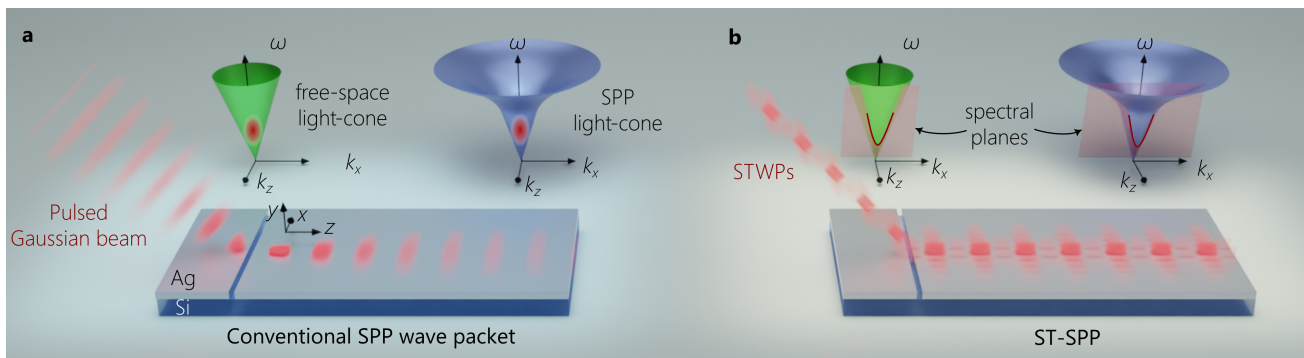


FIG. 1: **Comparison of SPPs and ST-SPPs at a metal-dielectric interface.** (a) Schematic of a free-space pulsed beam coupled to a conventional SPP wave packet bound to a metal-dielectric interface via scattering from a nanoslit in the metal surface. The sample is depicted here as a silver (Ag) layer atop a silicon (Si) substrate and clad by free space. The spectral support for the free-space pulsed beam is a 2D domain on the surface of the free-space light-cone $k_x^2 + k_z^2 = (\frac{\omega}{c})^2$, and that for the conventional SPP wave packet is a 2D domain on the surface of the SPP light-cone $k_x^2 + k_z^2 = k_{\text{SPP}}^2$. This conventional SPP wave packet undergoes both spatial diffractive spreading and temporal dispersive spreading. (b) Schematic of a free-space STWP coupled to an ST-SPP on the same sample as in (a). The spectral supports for the STWP and for the ST-SPP are curves at the intersection of a tilted spectral plane with the free-space light-cone and the SPP light-cone, respectively. The ST-SPP propagates invariantly on the metal surface without diffraction or dispersion.

Recently, free-space diffraction-free light sheets that travel along a straight line have been finally realized using a class of pulsed beams known as space-time wave packets (STWPs), which are diffraction-free without imposing a particular 1D transverse spatial profile [28]. Key to this unique feature is lifting the monochromaticity constraint, and then introducing a strict spectral association between the spatial and temporal frequencies undergirding the field spatiotemporal structure, thereby yielding unique characteristics such as propagation invariance in linear media [28–31], tunable group velocities independently of the medium refractive index [30, 32], self-healing upon traversing opaque obstacles [33], and anomalous refraction [34]. We have proposed a pulsed SPP beam (or SPP wave packet) that adapts the characteristic structure underpinning freely propagating STWPs to the particular setting of surface waves [35]. Because STWPs are the only propagation-invariant light sheets, they offer the potential for finally yielding diffraction-free SPPs that propagate along a straight line. By restricting the spatiotemporal spectrum of the SPP to the intersection of the SPP light-cone with a tilted spectral plane, one obtains a space-time SPP wave packet (ST-SPP) that inherits many of the unique propagation characteristics of STWPs; in particular, ST-SPPs propagate in a straight line without diffraction or dispersion at a metal-dielectric interface at a group velocity that may be tuned above (superluminal) or below (subluminal) that of a conventional SPP wave packet [35, 36]; see Fig. 1b. However, experimentally realizing an ST-SPP and ascertaining its propagation characteristics offers up a host of challenges. Because the typical decay length due to ohmic losses on a metal surface is lim-

ited to tens of microns [37–39], unambiguously monitoring the propagation of a pulsed SPP necessitates utilizing a broadband ultrashort pulse of width < 20 fs, which then raises the question of coupling a broadband spatiotemporally structured optical field to a surface-bound field [40].

Here we observe for the first time diffraction-free ST-SPPs traveling along a straight path with tunable group velocity at a metal-dielectric interface, which is made possible by resolving the multi-dimensional experimental challenge outlined above. First, we make use of ultrashort pulses of width 16-fs pulses (110-nm bandwidth), which correspond to an SPP of axial extent $\approx 3.6 \mu\text{m}$, thereby enabling the monitoring of their propagation over a short distance, and thus enabling us to confirm the tunability of the ST-SPP group velocity above and below that of an SPP as determined by its intrinsic dispersion. Second, we make use of a nano-slit milled into the metal surface for efficient broadband coupling of STWPs from free space to an ST-SPP (predicted theoretically [35, 41] and demonstrated with minimally structured fields [42]), while maintaining the structure of the target spatiotemporal spectrum. Third, the use of ultrashort pulses plays a crucial role in the phase-sensitive detection of the spatially and temporally resolved surface-bound field through two-photon fluorescence excited by a reference pulse interfering with the evanescent tail of the SPP at the metal surface. We thus reconstruct the surface-bound field for a variety of ST-SPPs, in addition to conventional SPP wave packets, and verify the details of their spatiotemporal structure, including a predicted signature tilt in their phase front with respect to the propagation direction. Furthermore, by exciting con-

ventional SPP wave packets and ST-SPPs of the same bandwidth, we confirm the diffractive spreading of the former and the diffraction-free propagation of the latter. These results establish a new form of SPP wave packets that offers unprecedented control over their propagation characteristics. This may enable novel applications in enhanced surface nonlinear optical interactions mediated by the tunable group velocity of ST-SPPs, in generating radiation through accelerating ST-SPPs [43], and launching isolated propagating topological SPP spin textures [13, 44, 45] or SPPs endowed with transverse orbital angular momentum [46, 47].

THEORETICAL FORMULATION

Spectral representation of ST-SPPs. The conceptual formulation of ST-SPPs is best understood by visualizing their spectral representation on the surface of the light-cone. For $(2 + 1)$ D pulsed optical fields restricted to one transverse dimension x in addition to the axial dimension z , the light-cone is the geometric representation of the dispersion relationship involving the transverse wave number k_x (or spatial frequency), the longitudinal wave number k_z , and the temporal frequency ω . In free space, the light-cone is $k_x^2 + k_z^2 = (\frac{\omega}{c})^2$, and that for an SPP at a metal-dielectric interface is $k_x^2 + k_z^2 = k_{\text{SPP}}^2(\omega)$; where c is the speed of light in vacuum, $k_{\text{SPP}} = \frac{\omega}{c} \sqrt{\frac{\epsilon_m \epsilon_d}{\epsilon_m + \epsilon_d}}$, and ϵ_m and ϵ_d are the relative permittivities of the metal and dielectric, respectively (Fig. 1a). In free space, where a $(2 + 1)$ D pulsed beam (or wave packet) takes the form of a light-sheet that is uniform along y and localized along x , its spectral support is a two-dimensional (2D) region on the surface of the free-space light-cone (Fig. 1a). Such a light-sheet undergoes diffractive spreading with free propagation. A conventional SPP wave packet is a $(2+1)$ D surface wave with finite transverse-spatial extent along x in addition to surface localization along y , whose spectral support in turn corresponds to a 2D region on the surface of the SPP light-cone (Fig. 1a) [35, 48]. This conventional SPP wave packet undergoes both diffractive spreading in space and dispersive spreading in time.

Ideal STWPs are pulsed beams that propagate rigidly in linear media without diffraction or dispersion, and whose propagation characteristics can be tuned largely independently of the material parameters [23, 28]. Rather than the 2D spectral support on the free-space light-cone associated with conventional pulsed light sheets, the spatiotemporal spectrum of an STWP is restricted to a 1D curve (a conic section) at the intersection of the light-cone with a plane that is parallel to the k_x -axis and makes an angle θ with the k_z -axis (Fig. 1b) [28]. This plane, $\omega - \omega_o = (k_z - k_o)c \tan \theta$, results in a straight-line spectral projection onto the $(k_z, \frac{\omega}{c})$ -plane, which indicates a fixed group velocity $\tilde{v} = c \tan \theta$ and the absence of dispersion to all orders [49]; here ω_o is a fixed carrier frequency, and $k_o = \frac{\omega_o}{c}$ is its associated wave

number. Moreover, the one-to-one association between ω and $|k_x|$ guarantees diffraction-free propagation of the time-averaged intensity [23]. Similarly for ST-SPPs, their spectral support as shown in Fig. 1b is also a 1D curve at the intersection of the SPP light-cone with the plane $\omega - \omega_o = (k_z - k'_o)\tilde{v}_{\text{SPP}} \tan \theta$, where \tilde{v}_{SPP} is the group velocity of a plane-wave pulsed SPP at $\omega = \omega_o$, and k'_o is the SPP wave number at ω_o [35]. The spectral projection onto the $(k_z, \frac{\omega}{c})$ -plane for the ST-SPP is also a straight line, indicating that – in addition to being diffraction-free – ST-SPPs propagate dispersion-free at a group velocity $\tilde{v} = \tilde{v}_{\text{SPP}} \tan \theta$ despite the intrinsic GVD associated with freely propagating SPPs (Fig. 1b) [35].

We show in Fig. 2 (first row) the spectral support for a conventional SPP wave packet on the SPP light-cone (Fig. 2a), its spectral projections onto the $(k_x, \frac{\omega}{c})$ and $(k_z, \frac{\omega}{c})$ planes (Fig. 2b,c), along with the out-of-plane field profile (Fig. 2d). We assume a separable Gaussian spectrum in space and time, and take into account the temporal bandwidth $\Delta\lambda \approx 110$ nm (FWHM) utilized in our experiments (Methods). Crucially, the phase front for this conventional SPP wave packet is orthogonal to the propagation axis z (Fig. 2d).

Producing an ideal ST-SPP with a bandwidth $\Delta\lambda = 110$ nm is prohibitive, as can be understood by considering a so-called ‘striped ST-SPP’ whose spatial profile results simply from the interference of a pair of plane waves with fixed spatial frequencies $\pm k_x$ (i.e., the field takes the transverse form $\cos k_x x$) [42]. Consequently a striped ST-SPP is separable with respect to space and time, and it thus does *not* offer the possibility of tuning the group velocity (indeed, its group velocity is $\tilde{v} \approx \tilde{v}_{\text{SPP}}$; Methods). We plot in Fig. 2a-c (second row) the spectral support for a striped ST-SPP, which is the intersection of iso- $|k_x|$ planes with the SPP light-cone. The out-of-plane field is separable, extended and periodic along x (with period $\lambda_x \equiv 2\pi/k_x = 10 \mu\text{m}$), and its phase front is orthogonal to the z -axis, leading to a lattice-like spatial distribution at any instant t (Fig. 2d).

A broadband ST-SPP is composed of a multiplicity of cosine SPPs with different k_x , each of which is associated with a prescribed ω , such that k_z is maintained in a linear relationship with ω . However, maintaining this linear relationship between k_z and ω over a large temporal bandwidth $\Delta\omega$ is prohibitive for SPPs because the curvature of the SPP light-line dictates a large accompanying spatial bandwidth Δk_x . Indeed, even if \tilde{v} remains within 1% of \tilde{v}_{SPP} , we still need $\frac{\Delta k_x}{k_o} \approx 0.23$ (with the parameters used in our experiments below) to maintain the spatiotemporal spectrum of an ideal ST-SPP over the large bandwidth $\Delta\lambda \approx 110$ nm used here. Because our experimental scheme conserves the spatial bandwidth Δk_x from free space to the surface-bound field, a large numerical aperture is therefore required. We define $k_x(\lambda) = \frac{2\pi}{\lambda} \sin\{\varphi(\lambda)\} = \frac{2\pi}{\lambda_x}$ in free space, where λ is the free-space wavelength, $\varphi(\lambda)$ is its propagation angle with the z -axis, and $\lambda_x = \lambda/\sin \varphi(\lambda)$ is the transverse period of the field along x . Our system is lim-

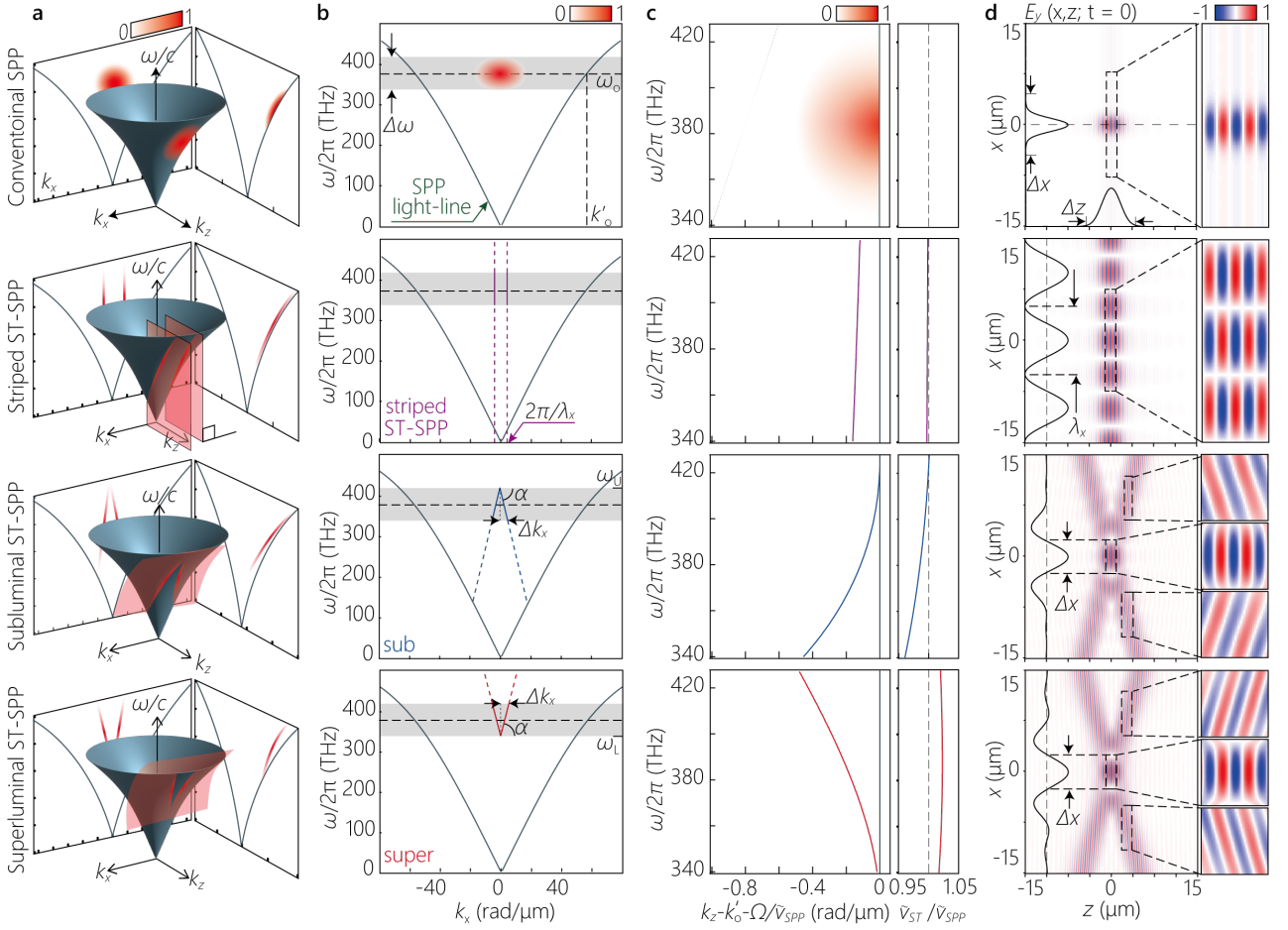


FIG. 2: Spectral representation of SPPs and ST-SPPs. (a) The spectral support on the surface of the SPP light-cone $k_x^2 + k_z^2 = k_{\text{SPP}}^2$ in $(k_x, k_z, \frac{\omega}{c})$ -space (shown in red). (b) The projection of the spectral support in (a) onto the $(k_x, \frac{\omega}{c})$ -plane. This spectral projection is invariant upon coupling the field from free space to the metal-dielectric interface (as a consequence of conservation of energy and transverse momentum). The gray band corresponds to the bandwidth $\Delta\omega$ of the laser pulse used in our experiments, and the dashed horizontal line is at $\frac{\omega_0}{2\pi} \approx 375$ THz ($\lambda_0 \approx 800$ nm in free space). (c) The spectral projection onto the $(k_z, \frac{\omega}{c})$ -plane after implementing $k_z \rightarrow k_z - k'_0 - \frac{\Omega}{\tilde{v}_{\text{SPP}}}$ for clarity, where $\Omega = \omega - \omega_0$. The panel to the right shows the group velocity of the wave packet $\tilde{v} = \frac{d\omega}{dk_z}$ normalized to \tilde{v}_{SPP} . The spectral range on the vertical axis corresponds to the bandwidth of the laser pulse. (d) The calculated out-of-plane real part of the field distribution $E_y(x, y, z; t)$ at $y = 0$ and $t = 0$ (Methods). The black curves on the left and bottom are cross-sections at $z = 0$ and $x = 0$, respectively. The right panels show magnified views of the dashed squares in the left panel, highlighting the structure of the phase fronts. The first row corresponds to a conventional SPP wave packet with $\Delta x = 9 \mu\text{m}$; the second to a striped ST-SPP with $\lambda_x = 10 \mu\text{m}$; the third to a subluminal ST-SPP with $\Delta x = 5 \mu\text{m}$; and the fourth to a superluminal ST-SPP with $\Delta x = 5 \mu\text{m}$.

ited to a maximum angular acceptance $\varphi_{\text{max}} \approx \pm 5^\circ$, a numerical aperture (NA) of ≈ 0.09 , which restricts the minimum spatial feature size to $\approx 9 \mu\text{m}$ that falls considerably short of the requirement for an ideal ST-SPP over $\Delta\lambda = 110$ nm. To address this challenge, we have implemented a compromise regarding the structure of the *realized* ST-SPP with respect to an *ideal* ST-SPP: (1) we maintain the one-to-one correspondence between $|k_x|$ and ω that is necessary for diffraction-free propagation; (2) we maintain control over the group velocity \tilde{v} of the ST-SPP away from that for a conventional SPP \tilde{v}_{SPP} in both

the subluminal ($\tilde{v} < \tilde{v}_{\text{SPP}}$) and superluminal ($\tilde{v} > \tilde{v}_{\text{SPP}}$) regimes; however (3) we allow the spectral projection onto the $(k_z, \frac{\omega}{c})$ -plane to be curved such that it lies in the $(k_z, \frac{\omega}{c})$ -plane between the SPP light-line and the linear spectral projection for an ideal ST-SPP (Fig. 2c). Consequently, we can operate with the available system NA, but at the cost of vouchsafing the complete elimination of GVD. This is a minimal disadvantage in light of the short SPP propagation distance limited by ohmic losses.

The spectral support of the realized ST-SPP is still a 1D curve on the surface of the SPP light-cone, but this curve results from the intersection of the SPP light-cone with a curved planar surface (rather than a plane) designed to yield a V-shaped spectral projection onto the $(k_x, \frac{\omega}{c})$ -plane [50]. For a subluminal ST-SPP ($\tilde{v} < \tilde{v}_{\text{SPP}}$), this projection takes the form $\omega - \omega_U = c|k_x| \tan \alpha$, where $\omega_U = \omega_o + \frac{\Delta\omega}{2}$ is the maximum frequency, $\omega < \omega_U$, α is the angle with the k_x -axis, and $\tan \alpha < 0$. For a superluminal ST-SPP ($\tilde{v} > \tilde{v}_{\text{SPP}}$), we have $\omega - \omega_L = c|k_x| \tan \alpha$, where $\omega_L = \omega_o - \frac{\Delta\omega}{2}$ is the minimum frequency, $\omega > \omega_L$, and $\tan \alpha > 0$. In both cases, ω_o is the central frequency, so that $\omega_o - \frac{\Delta\omega}{2} < \omega < \omega_o + \frac{\Delta\omega}{2}$. This curved surface remains parallel to the k_x -axis, but its projection onto the $(k_z, \frac{\omega}{c})$ -plane is no longer a straight line and is instead a curve that remains closer to the SPP light-line than in the case of the ideal ST-SPP (to remain within the system NA). The analytical relationship between ST-SPP group velocity \tilde{v} and the angle α is derived in Methods. The GVD coefficient for a conventional SPP wave packet in this case is $2.5 \times 10^3 \text{ fs}^2/\text{mm}$, and is 2.5×10^3 , 2.3×10^2 , and $2.0 \times 10^2 \text{ fs}^2/\text{mm}$ for a striped ST-SPP (with $\lambda_x = 10 \mu\text{m}$), a subluminal ST-SPP (with $\alpha = -64.5^\circ$), and a superluminal ST-SPP (with $\alpha = 64.5^\circ$), respectively.

We plot in Fig. 2 the spectral representation for the subluminal ST-SPP (third row) and the superluminal ST-SPP (fourth row). Of particular interest is the spatial profile of the out-of-plane field for both ST-SPPs, which is no longer separable as a result of the non-separability of their spatiotemporal spectra. Instead, we observe an X-shaped profile reminiscent of free-space STWPs [49, 51]. Crucially, the direction of the phase fronts varies across the wave front. In the vicinity of the center $x = 0$, the phase front is orthogonal to the propagation axis. However, along the branches of the X-shaped profile, the phase fronts are *tilted* with respect to the z -axis. Crucially, the *sign* of this phase-front tilt switches between the subluminal and superluminal regimes, and the magnitude of the tilt angle increases with the deviation of \tilde{v} from \tilde{v}_{SPP} [52].

EXPERIMENTAL ARRANGEMENT

We sketch in Fig. 3a the optical arrangement for synthesizing free-space STWPs, launching them into ST-SPPs on a metal-dielectric interface via scattering from a nano-slit, and observing the propagation of surface-bound ST-SPPs via spatially and temporally resolved two-photon fluorescence produced from the interference of the ST-SPP with a free-space reference pulse. We start with pulses from a Ti:sapphire laser oscillator of bandwidth $\Delta\lambda \approx 110 \text{ nm}$ (FWHM), center wavelength $\lambda_o \approx 800 \text{ nm}$, and a 10-fs transform-limited pulse duration (FWHM). However, the measured pulse width at the sample surface is $\Delta T \approx 16 \text{ fs}$ (FWHM) because of residual chirp in the optical system.

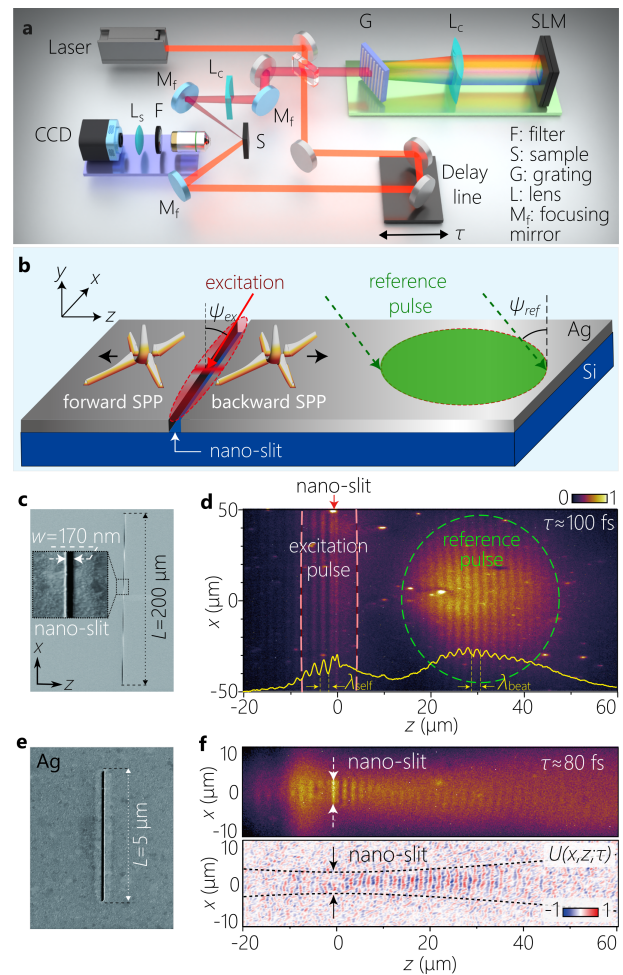


FIG. 3: Experimental arrangement for synthesizing, launching, and observing ST-SPPs. (a) Schematic of the setup for synthesizing free-space STWPs, launching them onto the sample, and imaging of the surface-bound field. (b) Schematic of the sample irradiation configuration. The STWP incidence angle is $\psi_{\text{ex}} = -45^\circ$ to the surface normal, and the reference pulse incidence angle is $\psi_{\text{ref}} = 45^\circ$. (c) SEM micrograph of the nano-slit milled into the Ag film. The inset shows a section of the nano-slit. (d) Two-photon fluorescence beat profile $I(x, z; \tau)$ at a fixed delay τ for a conventional SPP wave packet launched from the nano-slit. The yellow curve at the bottom is the axial profile $I(z; \tau) = \int dx I(x, z; \tau)$ at a fixed τ . The red arrow at the top indicates the nano-slit location. Dashed orange lines enclose the irradiation area of the excitation, and the dashed green circle encloses that for the reference pulse. (e) SEM micrograph of the 5- μm -long nano-slit used to launch a conventional SPP wave packet of that width. (f) The two-photon fluorescence beat pattern (upper panel) after irradiating the nano-slit in (e), and the extracted field $U(x, z; \tau)$ (lower panel), both at fixed delay $\tau \approx 80 \text{ fs}$. The dotted black curves correspond to the width of a Gaussian beam of width 5 μm ($1/e^2$ full width of the intensity), and serve as a guide for the eye.

Synthesis of ST-SPPs. The STWPs are synthesized from the pulsed laser via spatiotemporal spectral phase modulation as established in [28, 49]. The pulse spectrum is spatially resolved by a grating (300 lines/mm), the first diffraction order is selected and collimated using a cylindrical lens, which then impinges on a reflective, phase-only spatial light modulator (SLM); see Fig. 3a. This SLM imparts a 2D phase distribution to the incident wave front to deflect each wavelength λ by angles $\pm\varphi(\lambda)$ with respect to the z -axis, where $\sin\{\varphi(\lambda)\} = \pm(1 - \frac{\lambda}{\lambda_c}) \cot \alpha$. Here λ_c is the minimum ($\lambda > \lambda_c$) or the maximum ($\lambda < \lambda_c$) wavelength in the superluminal or subluminal regimes, respectively. The reflected phase-modulated wavefront is directed to a second grating identical to the first, whereupon the pulse is reconstituted to produce the STWP. For simplicity, the synthesis system in Fig. 3a is depicted as retro-reflecting from the SLM (whereupon the second grating coincides with the first); see Methods for details.

Sample preparation and launching ST-SPPs onto a metal-dielectric interface. The sample is a 100-nm-thick Ag film deposited on a silicon substrate. A crucial experimental challenge is to couple a broadband free-space STWP to a surface-bound ST-SPP at the metal-dielectric interface. We have recently examined theoretically an alternative approach to launching free-space STWPs into ST-SPPs that relies on scattering from a nano-slit in the metal surface (Fig. 3b) [41]. This coupling strategy retains a high efficiency over the bandwidth used here, and is thus preferable to conventional approaches for SPP coupling (e.g., gratings or evanescent prism-coupling) that modify the transverse wave number or do not operate over large bandwidths. Such a nano-slit conserves the transverse wave number $k_x^{\text{free}} = k_x^{\text{SPP}} = k_x$, where k_x^{free} and k_x^{SPP} are the transverse wave numbers for the free-space field and the launched SPP on either side of the nano-slit, respectively, so that the axial wave number is $k_z = \pm\sqrt{k_{\text{SPP}}^2 - k_x^2}$.

Two sets of 170-nm-wide, 100-nm-deep nano-slits were milled into the Ag film (Fig. 3c,e). One set of nano-slits has a lateral length of 200 μm and are used to launch ST-SPPs onto the Ag surface when illuminated with a free-space STWP (Fig. 3c). When illuminated with a conventional pulsed beam of large transverse extent along x , a conventional SPP wave packet is launched with a transverse width equal to that of the incident field (Fig. 3d). The second set of nano-slits has a reduced lateral length of 5 μm (Fig. 3e), and is used to launch conventional SPPs with a 5- μm -wide spatial profile (Fig. 3f). We have experimentally confirmed the efficacy of the nano-slit coupling methodology with striped ST-SPP [42], the spatiotemporally separable building blocks of ST-SPPs that comprise a single spatial frequency. Our results here confirm the theoretical predictions in [41] regarding the broadband coupling of STWPs to ST-SPPs. Finally, the sample is coated by a 30-nm-thick dye-doped PMMA film to form a two-photon fluorescent layer.

Spatiotemporal characterization of the ST-SPPs.

A portion of the initial laser pulse (20% by power) is split off to serve as a reference pulse, while the remainder (80 %) is directed to the above-described STWP synthesis system (Fig. 3a). The synthesized STWP that excites the ST-SPP is incident obliquely at an angle $\psi_{\text{ex}} = -45^\circ$ with respect to the sample normal, and is focused via a combination of spherical mirror and cylindrical lens onto the nano-slit, which launches it onto the sample surface (Fig. 3b; Methods) [42]. The incident free-space field is launched by the nano-slit in both the forward and backward directions [53, 54] (Fig. 3b). The reference pulse traverses an optical delay line τ and is then focused onto the metal surface away from the nano-slit to interact with the surface-bound SPP. The interference beat pattern of the SPP and the reference pulse excites two-photon fluorescence from the polymer layer [55]. Because we aim at detecting exclusively the interference of the reference pulse with the SPP, after eliminating any interference between the incident STWP excitation and the excited ST-SPP, we make use of the backward-coupled SPP ($z > 0$) rather than the stronger forward-coupled SPP ($z < 0$); see Fig. 3b.

RESULTS

Time-resolved measurements. We show in Fig. 3d the fluorescence profile of a conventional SPP wave packet with large transverse spatial profile excited by irradiating the nano-slit in Fig. 3c with a conventional pump pulse after setting the SLM phase to 0 everywhere; i.e., $\varphi(\lambda) = 0$. The beat profile to the left of the nano-slit ($z < 0$) results from self-interference of the launched SPP and the incident free-space excitation, which is thus stationary and independent of τ because the reference pulse is not involved. The two-photon fluorescence beat profile to the right is delimited by the irradiation area of the reference pulse on the sample surface (green dashed circle; focal spot $30 \times 60 \mu\text{m}^2$). The delay τ is adjusted to correspond to the propagating SPP wave packet reaching $z \sim 30 \mu\text{m}$. We define t as the time incurred by the surface-bound SPP (that travels at a group velocity \tilde{v}) to propagate from the nano-slit to the observation location. The time t will be different from the free-space delay τ placed in the path of the focused reference pulse (that travels at a group velocity $c/\sin\psi_{\text{ref}}$ along the metal surface) to reach the same location and produce the interference beat pattern; see Methods for the conversion between the delay τ and the time t .

We are now in a position to compare the time-resolved measurements of conventional SPP wave packets and ST-SPPs. We first investigate a conventional SPP wave packet where the initial laser pulses are focused onto the metal surface at the location of a 5- μm -long nano-slit (Fig. 3e). A conventional SPP wave packet is thus launched at the metal surface with a flat intensity profile, 5- μm transverse spatial width, and 16-fs temporal pulse width. The recorded two-photon fluorescence beat profile resulting from the launched SPP interfering with

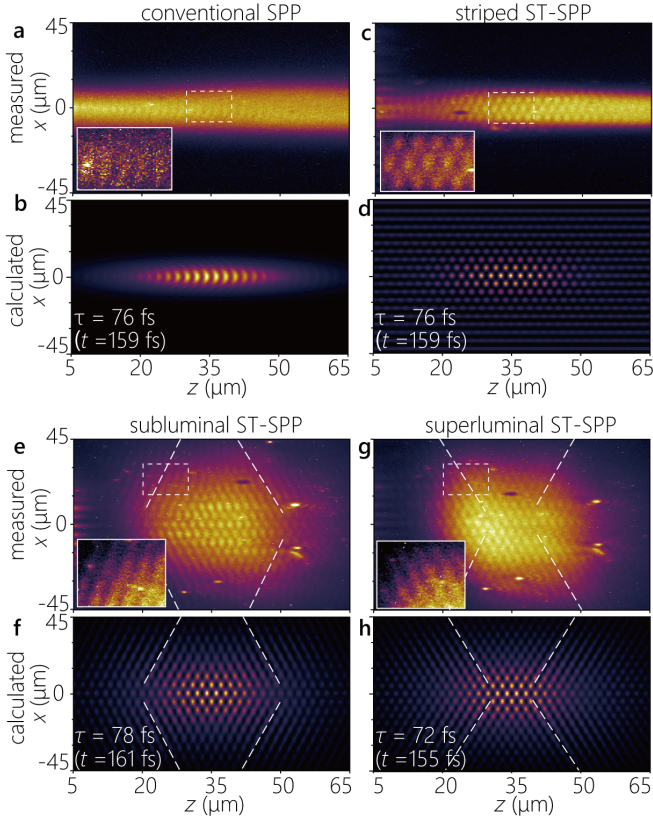


FIG. 4: Time-resolved two-photon fluorescence beat profiles for SPPs and ST-SPPs. (a) Measured two-photon fluorescence beat profiles $I(x, z; \tau)$ at a fixed delay τ produced by the interference of a conventional SPP wave packet (of transverse spatial width $5 \mu\text{m}$) with the reference pulse. Inset is a contrast-adjusted magnified view of the area enclosed in the dashed white rectangle ($10 \times 16 \mu\text{m}^2$) to highlight the flat wave front. (b) Calculated profile $I(x, z; \tau)$ corresponding to the measurement in (a); see Methods. (c,d) Same as (a,b) but for a striped ST-SPP with $\lambda_x \approx 10 \mu\text{m}$. (e,f) Same as (a,b) but for a subluminal ST-SPP; and (g,h) for a superluminal ST-SPP. The white dashed lines are guides for the eye representing the propagating wavefronts, and the insets highlight the tilted wave fronts at the edges of the ST-SPPs. All the two-photon fluorescence micrographs are acquired at a delay $\tau \approx 75 \text{ fs}$. The time t listed at the bottom left of the calculated profiles is that needed for each SPP to reach $z = 35 \mu\text{m}$ (Methods).

the reference pulse (focused spot size $60 \times 15 \mu\text{m}^2$) is shown in Fig. 3f. The intensity drops due to ohmic losses and diffractive spreading, and only a faint arc-shaped beat pattern is visible when the SPP wave packet reaches $z \sim 40 \mu\text{m}$. From this intensity profile we extract the SPP field distribution $U(x, z; \tau)$ plotted in Fig. 3g at fixed delay $\tau \approx 80 \text{ fs}$ (Methods).

In Fig. 4 we plot the experimentally recorded and the computed two-photon fluorescence beat profiles at a

fixed delay τ (Methods) for a conventional SPP of width $5 \mu\text{m}$ (Fig. 4a,b); a striped ST-SPP with transverse period $\approx 10 \mu\text{m}$ (Fig. 4c,d); a subluminal ST-SPP with $\alpha = -64.5^\circ$ (Fig. 4e,f); and a superluminal ST-SPP with $\alpha = 64.5^\circ$ (Fig. 4g,h). Computed spatiotemporal profiles capture all the key features of their measured counterparts. Crucially, the different phase front structures predicted in Fig. 2d are clearly observable, as depicted in the insets of the corresponding panels in Fig. 4. Whereas the conventional SPP has a flat phase front orthogonal to the z -axis (Fig. 4a,b, and Fig. 2d, first row), the striped ST-SPP has a checkered lattice-like structure (Fig. 4c,d, and Fig. 2d, second row). The phase front for the subluminal ST-SPP away from its center is tilted with respect to the z -axis (Fig. 4e,f, and Fig. 2d, third row). The sign of this phase-front tilt is reversed for the superluminal ST-SPP (Fig. 4g,h, and Fig. 2d, fourth row). The remaining quantitative differences between the computed and measured profiles in Fig. 4 are attributed to the residual chirp in the laser pulses, additional chirp encumbered in the STWP synthesis system, and spectral dissipation at the metal surface.

We have thus confirmed that the nano-slit is capable of launching free-space STWPs onto the metal surface as ST-SPPs, and that our experimental configuration can capture the time-resolved structure of the surface-bound, propagating ST-SPPs. We proceed to utilize this capability to verify two key features of ST-SPPs: their diffraction-free propagation, and the controllability of their group velocity (\tilde{v}) above and below that of a conventional SPP (\tilde{v}_{SPP}).

Diffraction-free propagation of ST-SPPs. To verify the diffraction-free behavior of the ST-SPPs, we evaluated the intensity profiles $I(x, z) = \int d\tau |U_{\text{beat}}(x, z; \tau)|^2$ at different axial positions by time-integration of the extracted field profiles $U_{\text{beat}}(x, z; t)$ obtained by removing background intensity from the two-photon fluorescence beat profiles (Methods). We plot in Fig. 5 the time-averaged intensity profiles for the striped ST-SPP (Fig. 5a), the subluminal ST-SPP (Fig. 5b), and the superluminal ST-SPP (Fig. 5c). For each case, we plot the intensity profiles obtained after focusing the reference pulse at two different axial positions along the sample surface: at $z \approx 35 \mu\text{m}$ and $z \approx 85 \mu\text{m}$ measured from the location of the nano-slit.

In contrast to a conventional SPP wave packet whose profile diffracts rapidly with propagation (Fig. 3f), the profiles of the ST-SPPs remain unchanged over the same propagation distance. In the case of the striped ST-SPP, this is to be expected because it contains only a single transverse wave number (i.e., an extended cosine wave profile). The limited transverse profile is a result of the narrow reference pulse irradiation spot utilized at the sample surface. The intensity profiles in Fig. 5a demonstrate that the striped ST-SPP maintains the same profile over a range of $\approx 5 \times$ the Rayleigh range ($z_R \approx 18.2 \mu\text{m}$; Methods). The transverse profiles of the subluminal (Fig. 5b) and superluminal (Fig. 5c) ST-SPPs

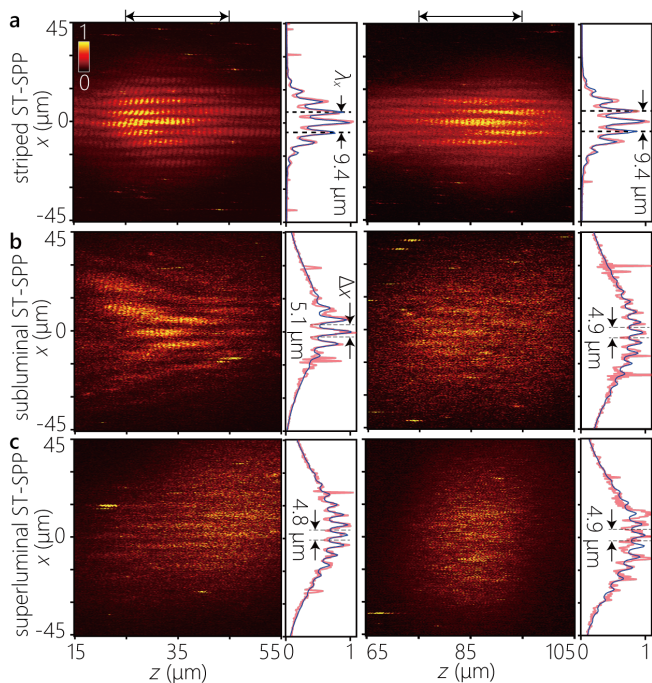


FIG. 5: Diffraction-free propagation of ST-SPPs.

We plot the measured time-averaged intensity profiles for (a) a striped ST-SPP, (b) a subluminal ST-SPP, and (c) a superluminal ST-SPP. Time-averaged intensity profiles $I(x, z; \tau)$ are measured at two locations for the reference pulse. The left panel corresponds to the reference pulse focused near the nano-slit at $15 < z < 55 \mu\text{m}$ (with delay in the range $\tau \approx 20 - 130$ fs), and the right panel to the reference pulse focused away from it at $65 < z < 105 \mu\text{m}$ ($\tau \approx 130 - 230$ fs). The intensity profiles $I(x)$ plotted to the right of each panel are obtained by axial integration $I(x) = \int dz I(x, z)$ over the range identified by the black arrows on top (red curves), along with least-square fits (blue curves). The overall intensity distribution of the fluorescence profiles are affected by the irradiated region of the reference light. The Rayleigh ranges for the corresponding beam waists are $18.2 \mu\text{m}$ for the striped ST-SPP and $21 \mu\text{m}$ for the superluminal and subluminal ST-SPPs, respectively.

are also maintained over the distance examined, which is over $\approx 4 \times$ Rayleigh lengths (the Rayleigh length is $z_R \approx 21 \mu\text{m}$). In all cases, the integrated cross-section along x plotted in the right panel are reasonably fitted by the (superposition) of Gaussian functions (representing the focused spot of the reference pulse) and the square of the sinusoidal-Gaussian function (representing the ST-SPP). The propagation distance here is limited by the ohmic losses. It is expected that the diffraction-free behavior extends significantly beyond $4z_R$, which can become manifest by increasing the NA and reducing the width Δx of the ST-SPP (reducing z_R significantly below the loss-restricted propagation distance).

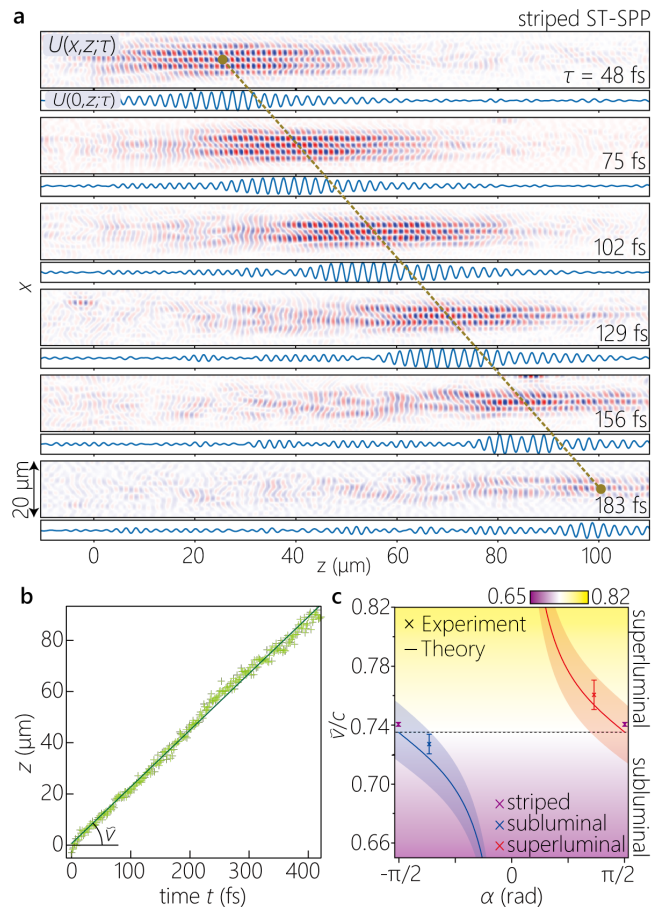


FIG. 6: Tuning the group velocity of ST-SPPs.

(a) The real part of the extracted field profiles $U(x, z; \tau)$ for a striped ST-SPP at different delays τ (listed on the right). We plot underneath each profile the longitudinal section $U(x=0, z; \tau)$. Each peak position was obtained by least-square fitting with a sinusoidally modulated Gaussian wave packet. (b) The axial center coordinate z of the peak of the intensity beat-profile from (a) plotted as a function of real time t (of the propagating striped ST-SPP) calculated from the external delay time τ (of the reference pulse; Methods). The corresponding range of the values of the delay is $\tau = 0 - 200$ fs. (c) Measured and calculated group velocities for the ST-SPPs (striped, superluminal, and subluminal). The solid curves are the calculated group velocities for ST-SPPs with $\Delta x = 5 \mu\text{m}$. The uncertainty bands surrounding the theoretical curves \tilde{v} result from a ± 2.5 -nm uncertainty in the thickness of the 30-nm-thick fluorescent PMMA layer.

Tuning of the group velocity of ST-SPPs. A unique feature of ST-SPPs is the possibility of tuning their group velocity by modifying only the structure of their spatiotemporal spectrum – without changing the sample itself. The group velocities of the ST-SPPs were estimated by examining a sequence of time-resolved two-photon fluorescence beat profiles. An example is shown in Fig. 6a

corresponding to the striped ST-SPP. For different values of the relative delay τ , we extract the field structure $U(x, z; \tau)$ and then fit (in the least-square sense) a sinusoidally modulated Gaussian function to the axial field $U(0, z; \tau)$ at each τ (Fig. 6a). We take the peak of this fitted function to be the axial center-of-weight z of the propagating ST-SPP. The delay τ was converted into propagation time t of the ST-SPP on the metal surface by factoring in that the surface-bound ST-SPP travels at a group velocity \tilde{v} , whereas the reference pulse travels at $c/\sin\psi_{\text{ref}}$ along the surface (Methods). We plot in Fig. 6b the measured axial positions z of the striped ST-SPP with real time t , and the estimated slope yields the group velocity $\tilde{v}_{\text{SPP}} = (2.22 \pm 0.004) \times 10^8$ m/s ($0.74c$), which is consistent with the group velocity of a conventional SPP $\tilde{v}_{\text{SPP}} = 2.22 \times 10^8$ m/s obtained from the first derivative of the dispersion curve of the SPP mode at the PMMA-coated Ag surface.

We repeated the procedure for the subluminal and superluminal ST-SPPs, and the estimated group velocities are $\tilde{v}_- = (2.18 \pm 0.02) \times 10^8$ m/s ($\approx 0.73c$) and $\tilde{v}_+ = (2.28 \pm 0.03) \times 10^8$ m/s ($\approx 0.76c$), respectively. The relative relationships of the measured group velocities $\tilde{v}_- < \tilde{v}_{\text{SPP}} < \tilde{v}_+$ are thus consistent with theoretical expectations and with the wavefront tilts in the two-photon fluorescence beat patterns in Fig. 4. We plot in Fig. 6c the measured group velocities compared to \tilde{v} calculated as a function of the opening angle α after taking into consideration the uncertainty resulting from the finite accuracy of determining the thickness (30 ± 2.5 nm) of the fluorescent PMMA layer.

DISCUSSION

We have confirmed that broadband ST-SPPs with complex separable and non-separable spatiotemporal structures can be excited at a metal-dielectric interface from a free-space STWP via a nano-slit milled into the metal surface. By appropriately sculpting the free-space spatiotemporal spectrum, we synthesized a variety of ST-SPP structures, monitored the time-resolved surface-bound fields, observed their signature wave-front tilt, confirmed their diffraction-free propagation along a straight line, and verified that their group velocity \tilde{v} can be tuned above (superluminal) and below (subluminal) that of a conventional SPP wave packet having the same bandwidth. The detection scheme developed here may be useful investigating the temporal evolution of light-matter interaction of structured light on small lengths and time scales. By demonstrating the feasibility of launching broadband ST-SPPs at a metal-dielectric interface, this proof-of-principle experiment thus extends the frontier of the burgeoning field of spatiotemporally structured optical fields into plasmonics and surface waves in general, including potentially water waves and surface acoustic waves.

A plethora of avenues for further investigation can

now be pursued. The experimental arrangement is so far limited by the numerical aperture within the paraxial regime. An immediate extension would involve increasing the numerical aperture of the free-space synthesis system, thereby increasing the spatial bandwidth of the STWP, resulting in stronger focusing of the excited ST-SPPs, with wavelength-scale and potentially sub-wavelength scale transverse spatial width [35]. Here, the unique advantages of ST-SPPs with regards to diffraction-free propagation become more pronounced, potentially reaching $\sim 300 \times z_{\text{R}}$ for $\Delta x \approx 3 \mu\text{m}$ (reaching $1/e$ of its initial on-axis peak value at $z = 2100z_{\text{R}}$) [35]. Another improvement in field localization can be achieved in the unique context of SPPs. The central spatial feature of the ST-SPP rides atop a broad pedestal, which drops significantly as we increase the spectral uncertainty undergirding the launched free-space STWP [23]. In previous work in free space, efforts have been devoted to *reducing* the spectral uncertainty in order to *increase* the propagation distance L_{max} . This is not a pressing concern here for ST-SPPs (as it is for free-space optical communications, for example) in light of the typical SPP decay lengths [35, 52]. As long as $L_{\text{max}} \sim 40 \mu\text{m}$, one may increase $\delta\lambda$ accordingly and thus substantially reduce the background term in the time-averaged intensity [23].

Recent studies have shown that structured SPPs can possess both in-plane and out-of-plane spin angular momentum [56, 57], which raises the intriguing possibility of structured SPP wave packets such as ST-SPPs having three-dimensional spin textures [52], and hence the potential for observing the interaction between structured SPPs and electron spin in magnetic materials. Another intriguing possibility is to exploit axial acceleration of ST-SPPs [58] in contrast to transverse acceleration of SPPs [43] induced by curved Airy beams is envisioned as a potential route for inducing radiation from the metal surface. Finally, our work opens new avenues for combining spatiotemporally structured light with the field localization associated with nanophotonics. The tunable group velocity of the ST-SPPs (which also includes a negative- \tilde{v} regime [35]) may enable phase-matching of nonlinear effects in thin films. Finally, ST-SPPs can be designed to become omni-resonant [59] with surface Fabry-Pérot cavities [60], such that the full bandwidth of broadband ST-SPPs couples to a single axial resonant mode. This raises the possibility of resonant – yet broadband – field enhancement at the metal interface for surface-enhanced Raman scattering (SERS) detection of molecules and pathogens.

REFERENCES

- [1] Zayats, A. V., Smolyaninov, I. I. & Maradudin, A. A. Nano-optics of surface plasmon polaritons. *Phys. Rep.* **408**, 131–314 (2005).
- [2] Stockman, M. I. *et al.* Roadmap on plasmonics. *J. Opt.* **20**, 043001 (2018).

- [3] Anker, J. N. *et al.* Biosensing with plasmonic nanosensors. *Nat. Mater.* **7**, 442–453 (2008).
- [4] Zhang, Y. *et al.* Plasmonic tweezers: for nanoscale optical trapping and beyond. *Light Sci. Appl.* **10**, 59 (2021).
- [5] Berweger, S., Atkin, J. M., Olmon, R. L. & Raschke, M. B. Adiabatic tip-plasmon focusing for nano-raman spectroscopy. *J. Phys. Chem. Lett.* **1**, 3427–3432 (2010).
- [6] Umakoshi, T., Tanaka, M., Saito, Y. & Verma, P. White nanolight source for optical nanoimaging. *Sci. Adv.* **6**, eaba4179 (2020).
- [7] Haffner, C. *et al.* Low-loss plasmon-assisted electro-optic modulator. *Nature* **556**, 483–486 (2018).
- [8] Ono, M. *et al.* Ultrafast and energy-efficient all-optical switching with graphene-loaded deep-subwavelength plasmonic waveguides. *Nat. Photon.* **14**, 37–43 (2020).
- [9] Eppenberger, M. *et al.* Resonant plasmonic micro-racetrack modulators with high bandwidth and high temperature tolerance. *Nat. Photon.* **17**, 360–367 (2023).
- [10] Atwater, H. A. & Polman, A. Plasmonics for improved photovoltaic devices. *Nat. Mater.* **9**, 205–213 (2010).
- [11] Yang, B., Li, C., Wang, Z. & Dai, Q. Thermoplasmonics in solar energy conversion: Materials, nanostructured designs, and applications. *Adv. Mater.* **34**, 2107351 (2022).
- [12] Zhang, Z., Fang, Y., Wang, W., Chen, L. & Sun, M. Propagating surface plasmon polaritons: Towards applications for remote-excitation surface catalytic reactions. *Adv. Sci.* **3**, 1500215 (2016).
- [13] Dai, Y. *et al.* Plasmonic topological quasiparticle on the nanometre and femtosecond scales. *Nature* **588**, 616–619 (2020).
- [14] Zhang, D. *et al.* Coherent surface plasmon polariton amplification via free-electron pumping. *Nature* **611**, 55–60 (2022).
- [15] Dreher, P., Janoschka, D., Frank, B., Giessen, H. & Meyer zu Heringdorf, F. J. Focused surface plasmon polaritons coherently couple to electronic states in above-threshold electron emission. *Commun. Phys.* **6**, 15 (2023).
- [16] Bozhevolnyi, S. I., Volkov, V. S., Devaux, E., Laluet, J.-Y. & Ebbesen, T. W. Channel plasmon subwavelength waveguide components including interferometers and ring resonators. *Nature* **440**, 508–511 (2006).
- [17] Oulton, R. F., Sorger, V. J., Genov, D. A., Pile, D. F. P. & Zhang, X. A hybrid plasmonic waveguide for subwavelength confinement and long-range propagation. *Nat. Photon.* **2**, 496–500 (2008).
- [18] Jacob, Z., Alekseyev, L. V. & Narimanov, E. Optical Hyperlens: Far-field imaging beyond the diffraction limit. *Opt. Express* **14**, 8247–8256 (2006).
- [19] Poddubny, A., Iorsh, I., Belov, P. & Kivshar, Y. Hyperbolic metamaterials. *Nat. Photon.* **7**, 948–957 (2013).
- [20] High, A. A. *et al.* Visible-frequency hyperbolic metasurface. *Nature* **522**, 192–196 (2015).
- [21] Mekawy, A. & Alú, A. Hyperbolic surface wave propagation in mid-infrared metasurfaces with extreme anisotropy. *J. Phys. Photonics* **3**, 034006 (2021).
- [22] Durnin, J., Miceli, J. J. & Eberly, J. H. Diffraction-free beams. *Phys. Rev. Lett.* **58**, 1499–1501 (1987).
- [23] Yessenov, M., Hall, L. A., Schepler, K. L. & Abouraddy, A. F. Space-time wave packets. *Adv. Opt. Photon.* **14**, 455–570 (2022).
- [24] Lin, J. *et al.* Cosine-Gauss plasmon beam: A localized long-range nondiffracting surface wave. *Phys. Rev. Lett.* **109**, 093904 (2012).
- [25] Wei, S. *et al.* Singular diffraction-free surface plasmon beams generated by overlapping phase-shifted sources. *Opt. Lett.* **38**, 1182–1184 (2013).
- [26] Salandrino, A. & Christodoulides, D. N. Airy plasmon: a nondiffracting surface wave. *Opt. Lett.* **35**, 2082–2084 (2010).
- [27] Minovich, A. *et al.* Generation and near-field imaging of Airy surface plasmons. *Phys. Rev. Lett.* **107**, 116802 (2011).
- [28] Kondakci, H. E. & Abouraddy, A. F. Diffraction-free space-time light sheets. *Nat. Photon.* **11**, 733–740 (2017).
- [29] Bhaduri, B. *et al.* Broadband space-time wave packets propagating for 70 m. *Opt. Lett.* **44**, 2073–2076 (2019).
- [30] Hall, L. A. & Abouraddy, A. F. Canceling and inverting normal and anomalous group-velocity dispersion using space-time wave packets. *Laser Photon. Rev.* **17**, 2200119 (2023).
- [31] He, H., Guo, C. & Xiao, M. Nondispersive space-time wave packets propagating in dispersive media. *Laser Photon. Rev.* **16**, 2100634 (2022).
- [32] Bhaduri, B., Yessenov, M. & Abouraddy, A. F. Space-time wave packets that travel in optical materials at the speed of light in vacuum. *Optica* **6**, 139–146 (2019).
- [33] Kondakci, H. E. & Abouraddy, A. F. Self-healing of space-time light sheets. *Opt. Lett.* **43**, 3830–3833 (2018).
- [34] Bhaduri, B., Yessenov, M. & Abouraddy, A. F. Anomalous refraction of optical spacetime wave packets. *Nat. Photon.* **14**, 416–421 (2020).
- [35] Schepler, K. L., Yessenov, M., Zhiyenbayev, Y. & Abouraddy, A. F. Space-time surface plasmon polaritons: A new propagation-invariant surface wave packet. *ACS Photonics* **7**, 2966–2977 (2020).
- [36] Cho, E.-S. & Lee, S.-Y. Propagation-invariant space-time plasmonic pulse in subwavelength mim waveguide. *Nanomaterials* **14**, 425 (2024).
- [37] Gramotnev, D. K. & Bozhevolnyi, S. I. Plasmonics beyond the diffraction limit. *Nat. Photon.* **4**, 83–91 (2010).
- [38] Iqbal, T. Propagation length of surface plasmon polaritons excited by a 1d plasmonic grating. *Curr. Appl. Phys.* **15**, 1445–1452 (2015).
- [39] Yi, J.-M. *et al.* Probing coherent surface plasmon polariton propagation using ultrabroadband spectral interferometry. *ACS Photonics* **4**, 347–354 (2017).
- [40] Diouf, M. *et al.* Excitation of surface plasmon polaritons by diffraction-free and vector beams. *Appl. Opt.* **61**, 7469–7473 (2022).
- [41] Ichiji, N., Yessenov, M., Schepler, K. L., Abouraddy, A. F. & Kubo, A. Exciting space-time surface plasmon polaritons by irradiating a nanoslit structure. *J. Opt. Soc. Am. A* **41**, 396–405 (2024).
- [42] Ichiji, N. *et al.* Observation of ultrabroadband striped space-time surface plasmon polaritons. *ACS Photonics* **10**, 374–382 (2023).
- [43] Henstridge, M. *et al.* Synchrotron radiation from an accelerating light pulse. *Science* **362**, 439–442 (2018).
- [44] Lei, X. *et al.* Photonic spin lattices: Symmetry constraints for skyrmion and meron topologies. *Phys. Rev. Lett.* **127**, 237403 (2021).
- [45] Dreher, P. *et al.* Spatiotemporal topology of plasmonic spin meron pairs revealed by polarimetric photo-emission microscopy. *Adv. Photonics* **6**, 066007 (2024).
- [46] Spektor, G. *et al.* Revealing the subfemtosecond dynamics of orbital angular momentum in nanoplasmonic vortices. *Science* **355**, 1187–1191 (2017).

- [47] Hancock, S. W., Zahedpour, S., Goffin, A. & Milchberg, H. M. Free-space propagation of spatiotemporal optical vortices. *Optica* **6**, 1547–1553 (2019).
- [48] Lassaline, N. *et al.* Optical Fourier surfaces. *Nature* **582**, 506–510 (2020).
- [49] Kondakci, H. E. & Abouraddy, A. F. Optical space-time wave packets of arbitrary group velocity in free space. *Nat. Commun.* **10**, 929 (2019).
- [50] Hall, L. A. & Abouraddy, A. F. Free-space group-velocity dispersion induced in space-time wave packets by v-shaped spectra. *Phys. Rev. A* **104**, 013505 (2021).
- [51] Yessenov, M. *et al.* Space-time wave packets localized in all dimensions. *Nat. Commun.* **13**, 4513 (2022).
- [52] Ichiji, N. *et al.* Transverse spin angular momentum of a space-time surface plasmon polariton wave packet. *Phys. Rev. A* **107**, 063517 (2023).
- [53] Lalanne, P., Hugonin, J. P., Liu, H. T. & Wang, B. A microscopic view of the electromagnetic properties of sub-lambda metallic surfaces. *Sur. Sci. Rep.* **64**, 453–469 (2009).
- [54] Zhang, L., Kubo, A., Wang, L., Petek, H. & Seideman, T. Imaging of surface plasmon polariton fields excited at a nanometer-scale slit. *Phys. Rev. B* **84**, 245442 (2011).
- [55] Ichiji, N., Otake, Y. & Kubo, A. Femtosecond imaging of spatial deformation of surface plasmon polariton wave packet during resonant interaction with nanocavity. *Nanophotonics* **11**, 1321–1333 (2022).
- [56] Bliokh, K. Y. & Nori, F. Transverse spin of a surface polariton. *Phys. Rev. A* **85**, 061801 (2012).
- [57] Shi, P., Du, L., Li, C., Zayats, A., V & Yuan, X. Transverse spin dynamics in structured electromagnetic guided waves. *Proc. Natl. Acad. Sci. (USA)* **118**, e2018816118 (2021).
- [58] Hall, L. A., Yessenov, M. & Abouraddy, A. F. Arbitrarily accelerating space-time wave packets. *Opt. Lett.* **47**, 694–697 (2022).
- [59] Shiri, A., Yessenov, M., Aravindakshan, R. & Abouraddy, A. F. Omni-resonant space-time wave packets. *Opt. Lett.* **45**, 1774–1777 (2020).
- [60] Zhu, W. *et al.* Surface plasmon polariton laser based on a metallic trench Fabry-Perot resonator. *Sci. Adv.* **3**, e1700909 (2017).

DATA AVAILABILITY STATEMENT

The data that support the plots within this paper and other findings of this study are available from the corresponding author upon reasonable request.

CODE AVAILABILITY STATEMENT

The code to produce numerical results within this paper and other findings of this study are available from the corresponding author upon reasonable request.

ACKNOWLEDGMENTS

This work was supported by the JSPS KAKENHI (JP16823280, JP20J21825, JP22H05131, JP23H04575, JP23KJ0355); MEXT Q-LEAP ATTO (JPMXS0118068681); Nanotechnology Platform Project (JPMXP09F-17-NM-0068); by the Nanofabrication

Platform of NIMS and University of Tsukuba; and by the U.S. Office of Naval Research (ONR) under contracts N00014-17-1-2458 and N00014-20-1-2789.

COMPETING INTERESTS

The authors declare no competing financial interests.

METHODS

Calculating the SPP and ST-SPP electric-field distributions. The calculated profiles of the out-of-plane electric fields for the SPPs and ST-SPPs plotted in Fig. 2d assume a 100-nm-thick Ag film on a Si substrate, with a 30-nm-thick PMMA coating clad with free space. The SPP dispersion curve $k_{\text{SPP}}(\omega)$ was calculated using a model proposed by Pockrand [61], and employed the dielectric function for Ag proposed by Rakic *et al.* [62]. The measured refractive index of PMMA is $n \approx 1.53$ at the operating wavelength. We take throughout the pulse spectrum to be $\tilde{E}(\omega)$, which is the Fourier transform of the pulse profile $E(t) = \int d\omega \tilde{E}(\omega) e^{-i\omega t}$. We assume a Gaussian profile in time:

$$E(t) = E_o e^{-i\omega_o t} \exp\left(-\frac{t^2}{2\ln 2(\Delta T)^2}\right), \quad (1)$$

where $\Delta T = 10$ fs is the FWHM of the intensity profile, and $\frac{\omega_o}{2\pi} = 375$ THz.

In general, the out-of-plane field is given by:

$$E(x, z; t) = \iint dk_x d\omega \tilde{\psi}(k_x, \omega) e^{i(k_x x + k_z z - i\omega t)}, \quad (2)$$

where $\tilde{\psi}(k_x, \omega)$ is the spatiotemporal spectrum, which is the Fourier transform of the initial field $E(x, 0; t)$. The first row in Fig. 2 corresponds to a conventional SPP wave packet, where $\tilde{\psi}(k_x, \omega)$ is separable, $\tilde{\psi}(k_x, \omega) = \tilde{\psi}(k_x) \tilde{E}(\omega)$; here $\tilde{\psi}(k_x)$ is the spatial spectrum of the excited SPP and assumed also to have a Gaussian profile.

The second row in Fig. 2 corresponds to a striped ST-SPP. The spatiotemporal spectrum is once again separable, $\tilde{\psi}(k_x, \omega) = \{\delta(k_x - k_{x0}) + \delta(k_x + k_{x0})\} \tilde{E}(\omega)$. The electric-field distribution is thus given by:

$$E(x, z; t) \propto \cos(k_{x0} x) \int d\omega \tilde{E}(\omega) e^{i(k_z(\omega) z - \omega t)}, \quad (3)$$

where the spatial frequency k_{x0} is fixed and is independent of ω , so that the transverse spatial DoF is separable with respect to the axial spatial and temporal DoFs. Consequently, the striped ST-SPP is diffraction-free (the transverse spatial profile does not change with propagation), but it is *not* localized.

The third and fourth rows in Fig. 2 correspond to subluminal and superluminal ST-SPPs, respectively. The spatiotemporal spectrum is no longer separable, in which

ω and $|k_x|$ are in one-to-one correspondence after selecting a value for the angle α . The field distribution for the ST-SPP is given by:

$$E(x, z; t) \propto \int d\omega \tilde{E}(\omega) \cos\{k_x(\omega)x\} e^{i\{k_z(\omega)z - \omega t\}}, \quad (4)$$

which is *not* separable with respect to the spatial and temporal DoFs. In all cases we have $k_z(\omega) = \sqrt{k_{\text{SPP}}^2(\omega) - k_x^2}$, and we take the same spectral profile $\tilde{E}(\omega)$ used above for the conventional SPP, the striped ST-SPPs, and the ST-SPPs.

Relationship between the spectral tilt angle θ and the opening angle α . We define the axial group velocity \tilde{v} of the ST-SPP in the usual way as $\tilde{v} = \left(\frac{dk_z}{d\omega}\bigg|_{\omega_o}\right)^{-1}$. For the V-shaped spectra realized here (Fig. 2a,b, third and fourth rows), tuning the opening angle α varies θ , and thus in turn \tilde{v} . For subluminal ST-SPPs we have $\omega - \omega_U = c|k_x| \tan \alpha$, where $\omega_U = \omega_o + \frac{\Delta\omega}{2}$ is the upper temporal frequency in the spectrum, $\omega < \omega_U$ and $\tan \alpha < 0$ ($-90^\circ < \alpha < 0$). The axial wave number is $k_z(\omega) = \sqrt{k_{\text{SPP}}^2(\omega) - k_x^2}$, and we make use of a Taylor expansion for $k_{\text{SPP}}(\omega)$: $k_{\text{SPP}} \approx k'_o + \frac{\Omega}{\tilde{v}_{\text{SPP}}} + \frac{1}{2}k_2\Omega^2$, where \tilde{v}_{SPP} and k_2 are the group velocity and GVD coefficient for a plane-wave pulsed SPP, respectively, and $k_x^2(\omega) = \left(\frac{\Omega - \Delta\omega/2}{c \tan \alpha}\right)^2$. We can thus write $k_z = \sqrt{A + 2B\Omega + C\Omega^2}$, where: $A = k_o'^2 - \frac{(\Delta k)^2}{4 \tan^2 \alpha}$, $B = \frac{k'_o}{\tilde{v}_{\text{SPP}}} + \frac{\Delta k}{2c \tan^2 \alpha}$, $C = k'_o k_2 + \frac{1}{\tilde{v}_{\text{SPP}}^2} - \frac{1}{c^2 \tan^2 \alpha}$, and $\Delta k = \frac{\Delta\omega}{c}$. We now have the following expression for the group velocity:

$$\tilde{v} = \left(\frac{dk_z}{d\Omega}\bigg|_{\Omega=0}\right)^{-1} = \frac{\sqrt{A}}{B}. \quad (5)$$

Defining a group index $\tilde{n} = \frac{c}{\tilde{v}} = \cot \theta$ for the ST-SPP and $\tilde{n}_{\text{SPP}} = \frac{c}{\tilde{v}_{\text{SPP}}}$ for a conventional SPP wave packet, we have:

$$\tilde{n} = \left(\tilde{n}_{\text{SPP}} + \frac{\Delta k/k'_o}{2 \tan^2 \alpha}\right) \left(1 + \frac{(\Delta k/k'_o)^2}{8 \tan^2 \alpha}\right), \quad (6)$$

so that $\tilde{n} > \tilde{n}_{\text{SPP}}$ ($\tilde{v} < \tilde{v}_{\text{SPP}}$) as expected for a subluminal ST-SPP.

For the superluminal ST-SPP we have $\omega - \omega_L = c|k_x| \tan \alpha$, where $\omega_L = \omega_o - \frac{\Delta\omega}{2}$ is the lower temporal frequency in the spectrum, $\omega > \omega_L$ and $\tan \alpha > 0$ ($0 < \alpha < 90^\circ$). The coefficients A and C are identical to those for the subluminal ST-SPP, and $B = \frac{k'_o}{\tilde{v}_{\text{SPP}}} - \frac{\Delta k}{2c \tan^2 \alpha}$, so that the group index for the ST-SPP is:

$$\tilde{n} = \left(\tilde{n}_{\text{SPP}} - \frac{\Delta k/k'_o}{2 \tan^2 \alpha}\right) \left(1 + \frac{(\Delta k/k'_o)^2}{8 \tan^2 \alpha}\right), \quad (7)$$

and to first order we have $\tilde{n} \approx (\tilde{n}_{\text{SPP}} - \frac{\Delta k/k'_o}{2 \tan^2 \alpha})$, $\tilde{n} < \tilde{n}_{\text{SPP}}$ ($\tilde{v} > \tilde{v}_{\text{SPP}}$) as expected for a superluminal ST-SPP.

Synthesizing free-space STWPs. The light source used in our experiments is a custom-built Ti:sapphire laser oscillator with a transform-limited pulse duration of

10 fs, center wavelength $\lambda_o = 800$ nm, FWHM-bandwidth $\Delta\lambda \approx 110$ nm, a repetition rate 90 MHz, and average power ≈ 400 mW. The spectrum is measured via a spectrometer (Ocean Optics HR4000) after coupling to an optical fiber with diameter 200 μm . Because of residual chirp in the optical system, the pulses are not transform-limited, and instead have a pulse duration of $\Delta T \approx 16$ fs at the sample surface. The pulse width is estimated by a home-built auto-correlator [55].

A portion of the laser power (20%) is reserved for subsequent use as a reference pulse. The remainder of the laser power (80%) is directed by a beam splitter to an optical system for synthesizing STWPs built along the lines described in [28]. The spectrum of the femtosecond pulse is spatially resolved by a grating (300 lines/mm), collimated by a cylindrical lens L_c (focal length $f = 250$ mm), and directed to a 2D phase-only, reflective SLM (Hamamatsu X13138-07). Each wavelength λ occupies a column of the SLM, along which the SLM imparts a spatial phase distribution $\pm \frac{2\pi}{\lambda} \sin\{\varphi(\lambda)\}x$. The overall 2D phase distribution imparted to the wave front corresponds to each wavelength being deflected by a prescribed propagation angle $\pm\varphi(\lambda)$ to yield the target relationship between k_x and λ . The reflected phase-modulated, spectrally resolved wavefront is directed to a second grating (identical to the first), whereupon the pulse is reconstituted to produce an STWP, which is then directed to the sample to excite an ST-SPP.

Sample fabrication. The sample was prepared by first depositing a 100-nm-thick Ag layer on a Si substrate via sputtering. The nanoslit structure was then milled into the Ag surface using a focused ion beam. The dimensions of the nanoslit are as follows: width $w = 170$ nm, depth $h = 100$ nm into the Ag layer, and extending across the sample by a length $L = 200 \mu\text{m}$ (Fig. 3c). These were used to excite the ST-SPPs, including the striped ST-SPPs, and the subluminal and superluminal ST-SPPs (Fig. 4, Fig. 6, and Fig. 5). This nano-slit was also used to excite the conventional plane-wave SPP wave packet (Fig. 3d). A second set of nano-slits was prepared with the same dimensions w and h , but with length $L = 5 \mu\text{m}$ (Fig. 1e). These nano-slits were used to excite conventional SPP wave packets with 5- μm -wide transverse profiles (Fig. 3f).

The full sample area was spin-coated with a 30-nm-thick poly(methyl methacrylate) (PMMA) layer doped with a laser dye (coumarin 343). The thickness of the coating was measured by spectral ellipsometry (Uvisel plus), from which we estimated an uncertainty in the coating thickness of ~ 5 nm. This in turn results in an uncertainty in estimating the SPP group velocity of $\sim 0.1 \times 10^8$ m/s.

SPP detection. Two wave packets overlap and interfere in the fluorescent polymer layer: the free-space incident reference pulse and the surface-bound SPP. The interference of these two wave packets produces a beat profile that excites two-photon fluorescence. The two-photon-fluorescence emission from the sample surface is collected with an objective lens (M Plan Apo SL20X,

Mitutoyo) equipped with a band-pass filter transmitting light in the range 475–495 nm (Semrock, FT-02-485/20-25), followed by a CCD camera (Rolera EM-C2, QImaging). The two-photon fluorescence signal is expected at a wavelength ≈ 490 nm from the dye used.

Calculating the SPP intensity profile. The intensity distribution $I(x, z; \tau)$ on the sample surface detected by the CCD camera is the time-average of the fourth power of the total electric field [55]:

$$I(x, z; \tau) = \int dt (|E_{\text{SPP}}(x, z; t) + E_{\text{free}}(x, z; t + \tau)|^2)^2; \quad (8)$$

Here, a proportionality constant is ignored because we are only interested in the relative intensity. The term E_{SPP} and E_{free} are the scalar field components of the excited SPP and the free-space fields, respectively, that overlap in the PMMA film. The interference of the two fields produces a spatial pattern having a spatial beat wavelength λ_{beat} given by:

$$\lambda_{\text{beat}} = \frac{2\pi}{|k_z - k_o \sin \psi_{\text{ref}}|}, \quad (9)$$

where $k_z(\omega_o, k_x)$ is the SPP axial wave number at $\omega = \omega_o$, and $k_o \sin \psi_{\text{ref}}$ is the in-plane axial wave number of the incident free-space field of the reference pulse. Similarly, the interference beat between the pump-probe pulse pair is $\lambda_{\text{light}} = \frac{2\pi}{|k_o \sin \psi_{\text{ex}} - k_o \sin \psi_{\text{ref}}|}$, where $k_o \sin \psi_{\text{ex}}$ is the in-plane axial wave number of the incident free-space field of the pump pulse. When employing ψ_{ex} and ψ_{ref} with the same signs to observe forward-coupling SPP, $\lambda_{\text{light}} \approx \lambda_{\text{beat}}$ if the values of ψ_{ex} and ψ_{ref} are comparable, making differentiation between them difficult. Consequently, we employed a contrasting configuration in which the signs of ψ_{ex} and ψ_{ref} are opposite of each other, such that λ_{light} is significantly less than λ_{SPP} , thereby facilitating their delineation.

Intensity profiles in Fig. 4 were calculated from the two-photon fluorescence signal resulting from the interference of the ST-SPP and the incident free-space conventional reference pulse. The intensity profile was calculated using Eq. 8 and assuming that both the ST-SPP and reference pulses are of width ≈ 16 fs as determined experimentally.

Removing the background. To extract the field distribution $U(x, z; \tau)$ from the measured two-photon fluorescence, we need to estimate experimentally the constants background. This is achieved by changing the delay τ in the path of the reference pulse by 2.7 fs, which corresponds to moving the excitation-reference interference beat profile by the laser carrier wavelength laser λ_o (a phase shift of 2π rad), and carrying out the time-resolved measurements. To obtain the background intensity, we first obtain the time-resolved field $U(x, z; \tau)$

from the interference beat profiles, and then obtain their average $\bar{U}(x, z; \tau)$ evaluated over an optical cycle:

$$\bar{U}(x, z; \tau) = \frac{1}{m} \sum_{i=1}^m U(x, z; \tau + (i-2) \times \frac{2.7}{m}). \quad (10)$$

In our work here, we have used $m = 2$ or 4 according to the exposure time used to avoid bleaching the fluorescence layer during laser irradiation. This averaging eliminates the excitation-reference oscillatory beat profile and extracts only the delay-independent background. This procedure assumes that minimal spatial change occurs in the SPP profile while advancing τ by 2.7 fs. By subtracting the averaged profile $\bar{U}(x, z; \tau)$ from the time-resolved profiles $U(x, z; \tau)$ we obtain the background-free profile of the pump-probe beat pattern at τ , $U_{\text{beat}}(x, z; \tau) = U(x, z; \tau) - \bar{U}(x, z; \tau)$. This procedure yields the field profile displayed in Fig. 3g, Fig. 6a.

Rayleigh range. The intensity distribution of the microscopic fluorescence beat images obtained via two-photon fluorescence are not proportional to the electric field intensity. We estimate the beam waist of the striped ST-SPP through obtaining λ_x by fitting the striped ST-SPP to a sinusoidal distribution along x . For a striped ST-SPP with $\lambda_x \approx 9.4 \mu\text{m}$, the beam waist is $2.15 \mu\text{m}$, corresponding to a Rayleigh range $z_R \approx 18.2 \mu\text{m}$ at a wavelength of 800 nm.

Group-velocity calculation. The two-photon fluorescence beat pattern is formed by the spatial overlap of the SPP propagating at a group velocity \tilde{v} and the reference pulse travelling along the sample surface at a group velocity $\tilde{v} = c/\sin \psi_{\text{ref}}$, where ψ_{ref} is the reference-pulse incident angle. We need to convert the external relative delay τ between the excitation and reference pulses to the propagation time t of the surface-bound SPP. As the SPP travels after a time t a distance $z_1 = \tilde{v}t$, whereas the delayed reference pulse travels a distance $z_2 = \frac{c}{\sin \psi_{\text{ref}}}(t - \tau)$. For the two wave packets to meet at $z_1 = z_2 = z_o$, and thus a two-photon fluorescence beat profile to be observed in the vicinity of z_o , we have $\tau = z_o(\frac{1}{\tilde{v}} - \frac{\sin \psi_{\text{ref}}}{c})$. This leads to the sought-after conversion $t = \tau(1 - \frac{\tilde{v}}{c} \sin \psi_{\text{ref}})^{-1}$. This conversion between t and τ was used in plotting Fig. 4 and Fig. 6b.

REFERENCES

- [61] Pockrand, I. Surface plasma oscillations at silver surfaces with thin transparent and absorbing coatings. *Surf. Sci.* 72, 577–588 (1978).
- [62] Rakić, A. D., Djurišić, A. B., Elazar, J. M. & Majewski, M. L. Optical properties of metallic films for vertical-cavity optoelectronic devices. *Appl. Opt.* 37, 5271–5283 (1998)